Letter | Editors' Suggestion

Impact of anharmonicity on the carrier mobility of the Pb-free $CsSnBr_3$ perovskite

Junwen Yin [1], Olle Hellman [2], and Samuel Poncé [1,3,*]

[1] *European Theoretical Spectroscopy Facility, Institute of Condensed Matter and Nanosciences, Université catholique de Louvain, Chemin des Étoiles 8, B-1348 Louvain-la-Neuve, Belgium*

[2] *Department of Molecular Chemistry and Materials Science, Weizmann Institute of Science, Rehovot 7610001, Israel*

[3] *WEL Research Institute, avenue Pasteur 6, 1300 Wavre, Belgium*

(Received 26 May 2025; revised 23 August 2025; accepted 10 October 2025; published 27 October 2025)

Charge carrier mobilities are critical parameters in halide perovskite solar cells, governing their average carrier velocity under an applied electric field and overall efficiency. Recent advances in first-principles calculations of electron-phonon interactions and carrier mobilities have enabled predictive computations for perovskite solar cells. However, the flexible octahedral frameworks and cationic displacements in these materials challenge the harmonic approximation, leading to significant difficulties in accurately calculating transport properties. To address these issues, we combine temperature-dependent effective potentials with the *ab initio* Boltzmann transport equations to compute carrier mobilities in a representative lead-free perovskite, $CsSnBr_3$. At room temperature, the electron (hole) Hall mobilities in $CsSnBr_3$ are 106 (256) $cm^2/(Vs)$ when neglecting anharmonic effects and 59 (145) $cm^2/(Vs)$ when included. This overestimation of the harmonic approximation arises from the neglect of scattering coming from soft modes. We provide a workflow for performing first-principles carrier mobility calculations in anharmonic systems, advancing the predictive modeling of perovskite solar cells.

DOI: 10.1103/yssy-5t2v

Halide perovskites are promising materials in optoelectronics [1,2], particularly for solar cells, LEDs, and photodetectors [3], due to their high absorption, long carrier diffusion, tunable band gap, and processability [4]. Lead-based perovskites like methylammonium and formamidinum lead halides ([MA,FA]PbX_3) are noted for their exceptional optoelectronic properties [5,6]. However, lead toxicity raises environmental and health concerns [5,6], driving interest in lead-free perovskites like tin-, germanium- and bismuth-based ones [7]. Carrier mobilities are vital for efficient lead-free perovskite solar cells but they are much lower than traditional semiconductors [8]. Low mobilities result from defects, ion migration, and grain boundary scattering [8–11]. Advancing lead-free perovskites involves optimizing material composition, reducing defects, and enhancing intrinsic properties to increase mobility and reduce losses [12,13]. Materials informatics has rapidly advanced, aiding in the discovery of new materials. Techniques like density functional perturbation theory (DFPT) [14,15], quantum Monte Carlo simulations [16], and *ab initio* molecular dynamic (aiMD) [17] are used to explore structural, compositional, and technological descriptors related to material performance. Perovskite materials often exhibit a strong local lattice disorder, which is often referred to as *polymorphous* [18–21] or beyond *naive-DFT* [22,23]. In such instances, a much larger supercell is constructed and the local geometry is allowed to relax while maintaining the overall macroscopic space group.

Anharmonic effects can also be treated directly in the primitive cell of the materials. Methods developed to tackle this include self-consistent phonon (SCP) [24,25], self-consistent-field nonperturbative methods with temperature-dependent atomic displacement [19,26], DFPT-based perturbative methods for third-order force constants [27,28], and aiMD methods [29]. SCP methods compute effective harmonic force constants in supercells. These forces can be sampled using the stochastic self-consistent harmonic approximation (SSCHA [24], SSCHA code [30]) or the temperature-dependent effective potential (TDEP [29,31], TDEP code [32]), both of which employ a stochastic framework for self-consistently determining anharmonic force constants. Alternatively, anharmonic forces can be obtained by Taylor expansion to the third order, which is applied in PHONOPY [33,34] and D3Q [35]. Another approach is the least absolute shrinkage and selection operator, also known as compressed sensing [36–39], which provides an efficient framework to extracting higher-order interatomic force constants. The self-consistent *ab initio* lattice dynamics method [40] iteratively solves the SCP equations to determine the phonon properties in anharmonic systems. These methods have been implemented in various software packages such as HIPHIVE [41], ZG [42], and A-TDEP [43]. However, few of these anharmonic methods have been used to compute the charged carrier transport properties. The two most common *ab initio* methods to compute transport properties are the Green-Kubo formula [44–46] or the iterative Boltzmann transport equation (BTE) [47,48]. In particular, the electron-phonon Wannier (EPW) code [49,50] can efficiently interpolate Hamiltonian, dynamical matrices, and electron-phonon matrix elements on dense momentum grids to solve the BTE. The Kubo-Greenwood approximation to Green-Kubo was recently used to calculate the carrier mobility of $SrTiO_3$ and $BaTiO_3$ using aiMD in the NVT canonical ensemble [51] and a charged carrier mobility expression based

*Contact author: samuel.ponce@uclouvain.be

on MD mean-square displacement was also used to study $MAPbI_3$ and $MAPbBr_3$ [52]. Furthermore, using the BTE, the electron drift mobility of cubic $SrTiO_3$ was studied with anharmonic effects [53,54], while the electron and hole drift mobilities in $CsSnI_3$ and $CsPbI_3$ were studied using compressed sensing [55].

We developed an interface between TDEP and EPW software to incorporate *partial* anharmonic effects in carrier transport calculations. Here, by *partial*, we mean that we use an updated effective interatomic force constant that includes anharmonic effects. Still, we compute the change of changes in the perturbed potential using DFPT [14], aligning with current methods [53]. This study calculates the temperature-dependent phonon dispersion, electron-phonon interactions, and carrier mobilities of $CsSnBr_3$, an inorganic perovskite with promising optoelectronic properties, including a suitable band gap and absence of toxic lead [56,57]. Its oxidation and instability make it ideal for further research to enhance mobility and stability via anharmonic lattice dynamics [55]. Using DFPT and TDEP, we obtained harmonic and anharmonic interatomic force constants (IFCs). We evaluate $CsSnBr_3$ mobility temperatures, finding anharmonicity reduces intrinsic Hall mobility with room-temperature electron and hole mobilities of 59 and 145 $cm^2/(Vs)$, respectively. Our investigation of the electronic structure and transport properties of halide perovskites was conducted using first-principles calculations within the framework of density functional theory (DFT) using the QUANTUM ESPRESSO (QE) package [58]. We use fully relativistic optimized norm-conserving Vanderbilt pseudopotentials [59] based on the Perdew-Burke-Ernzerhof (PBE) generalized gradient approximation [60] from the standard PSEUDODOJO library [61]. The plane-wave basis set was expanded with a kinetic energy cutoff of 80 Ry, and a $12 \times 12 \times 12$ **k**-point grid was used, ensuring convergence in energy with a tolerance of 10^{-11} Ry. The lattice parameters are optimized with PBE, including spin-orbit coupling (SOC), which gives a lattice parameter of 5.89 Å for the cubic phase. For the electronic band structure, we used the HSE06 hybrid functional [62] with a 0.17 fraction of Fock exchange [55] and a $6 \times 6 \times 6$ **k**-point grid. Harmonic phonon calculations are obtained using DFPT [14] with a $6 \times 6 \times 6$ **q**-point grid. The dielectric functions and Born effective charge tensor computed at $\mathbf{q} = \mathbf{\Gamma}$ require a dense $24 \times 24 \times 24$ **k**-point grid to be converged [see Fig. S1 of the Supplemental Material (SM) [63]]. To include anharmonic effects in the computations of phonon and electron-phonon coupling, we follow the TDEP method [29]. The total energy can be written using a Taylor expansion around the equilibrium Born-Oppenheimer (BO) atomic position $\{\mathbf{R}_0\}$:

$$E_0^{\mathrm{BO}}\{\mathbf{R}\} = E_0^{\mathrm{BO}}\{\mathbf{R}_0\} + \frac{1}{2}\sum_{\substack{\kappa\alpha \\ \kappa'\alpha'}} \frac{\partial^2 E_0^{\mathrm{BO}}\{\mathbf{R}\}}{\partial R_{\kappa\alpha}\partial R_{\kappa'\alpha'}}\bigg|_{\mathbf{0}} \times \Delta R_{\kappa\alpha}\Delta R_{\kappa'\alpha'} + O(\Delta\mathbf{R}^3), \tag{1}$$

where $\Delta R_{\kappa\alpha} = R_{\kappa\alpha} - R_{0\kappa\alpha}$ is the displacement of atom κ in the Cartesian direction α, and where $|_{\mathbf{0}}$ indicates that we are taking the derivatives at $\{\mathbf{R} = \mathbf{R}_0\}$. The second-order derivative with respect to atomic displacement is the interatomic force constant (IFC), denoted by $C_{\kappa\alpha\kappa'\alpha'}$. The IFC can be determined using linear response methods or finite difference, while the anharmonic higher-order terms are truncated.

The TDEP approach consists of finding an effective harmonic IFC that best describes the energy landscape felt by the nuclei oscillating around their equilibrium position at a given temperature. To achieve this, we use stochastic TDEP (sTDEP) [64] which selects atomic configurations drawn from a canonical ensemble corresponding to the (self-consistent) effective harmonic ensemble, including nuclear quantum effects [65]. To determine the effective force constant matrix $\tilde{C}$ that most accurately represents the real forces, we minimize the force difference over N configurations $\sum_i^N \frac{1}{N}\sum_\kappa |\mathbf{F}_\kappa - \tilde{\mathbf{F}}_\kappa|$, where $\mathbf{F}_\kappa$ is the DFT force on atom κ and $\tilde{\mathbf{F}}_\kappa$ is the effective force computed from $\tilde{F}_{\kappa\alpha} = \sum_{\kappa'\alpha'} \tilde{C}_{\kappa\alpha,\kappa'\alpha'}\Delta R_{\kappa'\alpha'}$. If the number of configurations exceeds three times the number of atoms, the system of equations for $\tilde{C}$ becomes overdetermined. We obtain the linear least-squares solution for $\tilde{C}$. After convergence with respect to the number of configurations, we define the force constant matrix at temperature T and use it to generate new stochastic displacements. We study $CsSnBr_3$ in its cubic phase stable above 292 K [66] and perform sTDEP calculations at 300, 350, 400, 450, and 500 K. Force constants are computed at 500 K for better convergence due to large displacements and used as initial guesses for lower temperatures. Each temperature requires seven iterations to converge phonon dispersions to 0.1 meV, with each iteration using $N = 2^l + 2^{(l-1)}$ configurations, depending on the iteration number l.

Electrons in semiconductors scatter under an electric field primarily due to phonons, which defines carrier mobility. We use the BTE in EPW to analyze semiconductor low-field mobility, calculating drift mobility $\mu_{\alpha\beta}$ from the electrical conductivity tensor $\sigma_{\alpha\beta}$ over carrier density n_c: $\mu_{\alpha\beta} = \frac{\sigma_{\alpha\beta}}{en_c}$. The tensor $\sigma_{\alpha\beta}$ describes the change in the carrier occupation function $f_{n\mathbf{k}}$ relative to the electric field $\mathbf{E}$, calculated as follows using [67]

$$\sigma_{\alpha\beta} = -\frac{e}{\Omega^{\mathrm{uc}}}\sum_n \int \frac{\mathrm{d}\mathbf{k}}{\Omega^{\mathrm{BZ}}} v_{n\mathbf{k}\alpha}\partial_{E_\beta} f_{n\mathbf{k}}, \tag{2}$$

where Ω^{BZ} is the Brillouin-zone volume, Ω^{uc} the unit-cell volume, $\partial_{E_\beta} f_{n\mathbf{k}}$ is the linear response of the carrier occupation function due to an external electric $\mathbf{E}$, given by [50,67,68]

$$\partial_{E_\beta} f_{n\mathbf{k}} = e v_{n\mathbf{k}\beta}\frac{\partial f^0_{n\mathbf{k}}}{\partial \epsilon_{n\mathbf{k}}}\tau_{n\mathbf{k}} + \frac{2\pi\,\tau_{n\mathbf{k}}}{\hbar}\sum_{m\nu}\int \frac{d\mathbf{q}}{\Omega^{\mathrm{BZ}}} |g_{mn\nu}(\mathbf{k},\mathbf{q})|^2 \times \Big[\big(n_{\mathbf{q}\nu} + 1 - f^0_{n\mathbf{k}}\big)\delta(\epsilon_{n\mathbf{k}} - \epsilon_{m\mathbf{k}+\mathbf{q}} + \hbar\omega_{\mathbf{q}\nu}) + \big(n_{\mathbf{q}\nu} + f^0_{n\mathbf{k}}\big)\delta(\epsilon_{n\mathbf{k}} - \epsilon_{m\mathbf{k}+\mathbf{q}} - \hbar\omega_{\mathbf{q}\nu})\Big]\partial_{E_\beta} f_{m\mathbf{k}+\mathbf{q}}, \tag{3}$$

where n denotes a Kohn-Sham band index, $\mathbf{k}$ is the electron wave vector, $\tau_{n\mathbf{k}}$ is the carrier relaxation time [47], $\partial_{E_\beta} f_{n\mathbf{k}}$ is a shorthand notation for $(\partial f_{n\mathbf{k}}/\partial E_\beta)|_{E=0}$, $v_{n\mathbf{k}\alpha} = \hbar^{-1}\partial\epsilon_{n\mathbf{k}}/\partial k_\alpha$ is the intraband velocity matrix element for the Kohn-Sham eigenvalue $\epsilon_{n\mathbf{k}}$, and δ denotes the Dirac delta function, $g_{mn\nu}(\mathbf{k},\mathbf{q})$ is the electron-phonon matrix element describing the interaction from the state $n\mathbf{k}$ to the state $m\mathbf{k}+\mathbf{q}$ via the phonon of branch ν and wave vector $\mathbf{q}$. The temperature enters this equation via the Fermi-Dirac and Bose-Einstein equilibrium distribution functions $f^0_{n\mathbf{k}}$ and $n_{\mathbf{q}\nu}$, respectively.

However, we note that often it is the Hall and not the drift mobility which is measured in experiment. To compute the Hall mobility, we add a vanishing finite magnetic field in Eq. (3) following Refs. [50,68]. In this work, we interpolated the electron-phonon matrix element to compute the drift and Hall mobility using $80 \times 80 \times 80$ fine $\mathbf{k}$ and $\mathbf{q}$ grids to reach convergence, shown in Fig. S2 of the SM [63] for the case of hole mobility.

The $CsSnBr_3$ perovskite transitions from monoclinic at low temperature to tetragonal at 247 K, and to cubic ($Pm\bar{3}m$, No. 221) at 292 K [66]. In the cubic phase, large Cs^+ ions fill the voids in the $SnBr_6$ octahedral framework. Anharmonicity, due to atomic displacements and $SnBr_6$ octahedra tilting, affects the material's thermal and vibrational properties. As shown in Eqs. (2) and (3), precise calculation of the electron-phonon matrix elements $g_{mn\nu}(\mathbf{k}, \mathbf{q})$ is necessary to consider anharmonic effects on electron-phonon interactions and carrier mobility, where [69]

$$g_{mn\nu}(\mathbf{k}, \mathbf{q}) = \sqrt{\frac{\hbar}{2\omega_{\mathbf{q}\nu}}} \sum_{\kappa\alpha} \frac{e_{\kappa\alpha,\nu\mathbf{q}}}{\sqrt{M_\kappa}} \langle \Psi_{m\mathbf{k}+\mathbf{q}} | V_{\mathbf{q}\kappa\alpha} | \Psi_{n\mathbf{k}} \rangle \quad (4)$$

with $V_{\mathbf{q}\kappa\alpha}$ the variation of the Kohn-Sham potential due to displacements of atom κ (with mass M_κ) in the Cartesian direction α. We use TDEP to calculate the anharmonic phonon energies $\omega_{\mathbf{q}\nu}$ and the eigenvectors $e_{\kappa\alpha,\mathbf{q}\nu}$, maintaining the deformation potential $V_{\mathbf{q}\kappa\alpha}$ at the harmonic level. Calculations with and without SOC are performed to account for heavy elements. Given the PBE functional's band gap underestimation, HSE06 hybrid functional calculations are also performed [62]. Phonon properties are assessed using both DFPT and TDEP to show anharmonicity effects. Electron-phonon interactions are interpolated with EPW and compared with DFPT results. Imaginary modes are excluded with a threshold of 5 cm^{-1}.

PBE calculations yield a lattice constant of 5.89 Å, compared to the measured 5.80 Å [56]. Figure 1 shows a direct band gap in cubic $CsSnBr_3$ at the R point in the Brillouin zone. The PBE-calculated band gap is 0.64 eV without SOC, dropping to 0.29 eV with SOC, both below the experimental cubic and tetragonal band gap ranging from 1.75 to 1.82 eV [57,70,71]. At the HSE06 level with SOC, it increases to 1.55 eV, aligning better with the experiments but still underestimating the experimental value, in line with recent findings [72]. Sn-Br bonds dominate the band edge character, with Cs contributing minimally. The conduction band edge is from antibonding between Br 6s and Sn 5p orbitals, while the valence band edge is from Br 5p and Sn 5s orbitals. Without SOC, the CBM is threefold degenerate, splitting into a doublet and a quadruplet with SOC. Here SOC is included in the electron-phonon interaction and carrier transport due to the band edge's importance for carrier mobility. However, we neglect the band renormalization [67,73] and assume the quasiparticle approximation to be valid [46,74].

Figure 2 compares the phonon dispersions calculated using DFPT and TDEP at 300 K, and we show the results for the other temperatures in the SM, Fig. S3 [63], where we observe a stiffening of the low-frequency modes with temperature. Both calculations account for the LO-TO splitting. Consistent with previous reports on perovskite structures [53,55], the harmonic results show negative frequencies at the R and

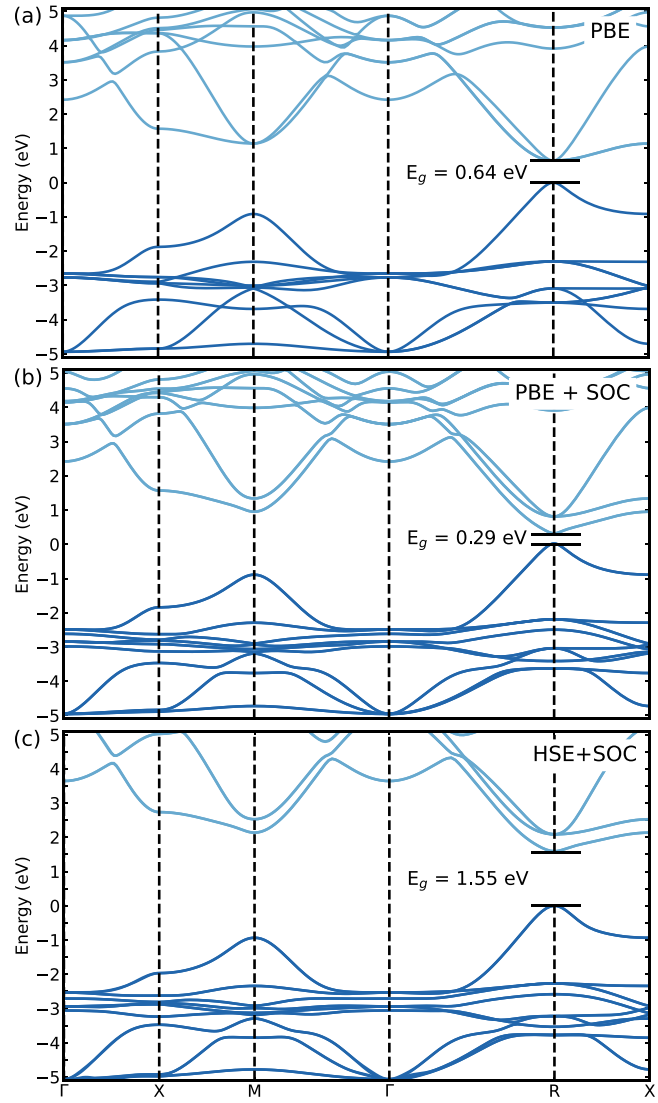

FIG. 1. Electronic band structures of cubic $CsSnBr_3$ (a) calculated with PBE without SOC, (b) with PBE with SOC, and (c) with HSE06 with SOC. The valence band maximum is set to zero as the reference energy level.

M points, indicating cation rattling and octahedral instability. In contrast, the results which include anharmonicity at 300 K eliminate these negative frequencies, stabilizing the soft phonons. Notably, the lowest-energy optical modes at the zone center more than double in frequency, while the highest-energy optical modes remain almost constant upon inclusion of anharmonicity. To integrate the TDEP IFCs into QE and EPW for electron-phonon interaction calculations, we map the spherical IFCs from EPW onto the edge-centered convention used by QE as shown in Fig. S6 of the SM [63]. Dipolar long-range interactions are removed and consistently readded during Fourier interpolation with identical Ewald parameters set in both codes [14,75].

We fit the band edges to a parabolic function and report the carrier effective mass in Table I. We compare the effective masses for $CsSnBr_3$ under PBE without SOC, PBE with SOC, and HSE06 with SOC. Our focus is on holes at the valence

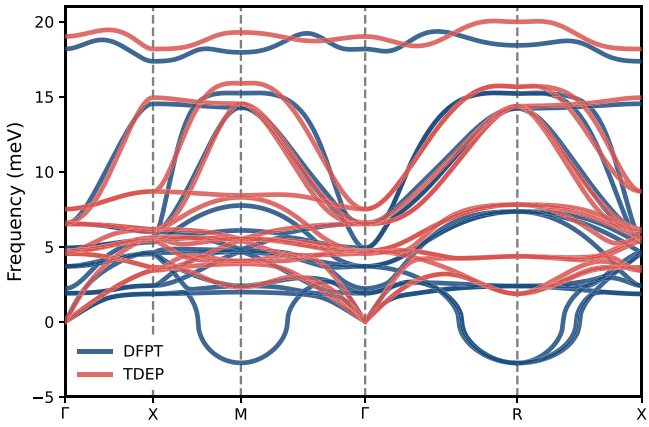

FIG. 2. Phonon band structures of cubic $CsSnBr_3$ where the blue lines show the harmonic results (DFPT) while the red lines show the anharmonic results (TDEP) at 300 K. The harmonic calculations was performed with a $6 \times 6 \times 6$ **q**-point grid and the anharmonic calculation using a $4 \times 4 \times 4$ supercell.

band maximum (VBM) and electrons at the conduction band minimum (CBM) at the R point. The VBM band dispersion is isotropic and parabolic. Hole effective masses m_h^*, ranging from 0.06 to 0.13, are consistently lower than electron effective masses m_e^*. The Drude mobility $\mu = \frac{e\tau}{m^*}$ indicates higher hole mobility than electron, a prediction supported by later transport calculations. The electron effective mass (m_e^*) discussion shows more complexity than m_h^*. Without SOC, the CBM is threefold degenerate, leading to heavy (m_{he}^*) and light (m_{le}^*) electron masses. Anisotropy in m_e^* depends on the measurement direction. For m_{le}^*, effective masses are similar in the (111) and (001) directions, being 0.08 and 0.05. m_{he}^* shows significant anisotropy, with the mass increasing from 0.27 in the (111) direction to 0.84 in the (001) direction. For $CsSnBr_3$, calculated results suggest holes move faster than electrons, confirmed by BTE transport results.

We use Wannier-Fourier interpolation [76] to efficiently solve the BTE. Initial guesses for Wannier functions include s orbitals on Cs and p on Sn and Br, resulting in 26 and 13 functions with and without SOC. As shown in Figs. S5 and S6 of the SM [63], these functions accurately reproduce the PBE band structure for both cases, allowing precise electron-phonon interaction calculations. The high cost of direct band structure calculations without interpolation prevents us from verifying HSE06. Effective masses in Table I are derived from the Wannier function interpolations. To evaluate the interpolation quality of the electron-phonon coupling matrix $|g_{mn\nu}(\mathbf{k}, \mathbf{q})|$, we compare direct DFPT calculations

TABLE I. Effective masses of cubic $CsSnBr_3$ in units of the electron rest mass along the (111) direction, corresponding to the R-Γ direction and the (001) direction corresponding to the R-X direction.

	PBE			PBE+SOC		HSE+SOC	
Direction	m_h^*	m_{le}^*	m_{he}^*	m_h^*	m_e^*	m_h^*	m_e^*
(111)	0.07	0.08	0.27	0.06	0.09	0.13	0.27
$(0\,\bar{1}\,\bar{1})$	0.07	0.05	0.84	0.06	0.08	0.13	0.22

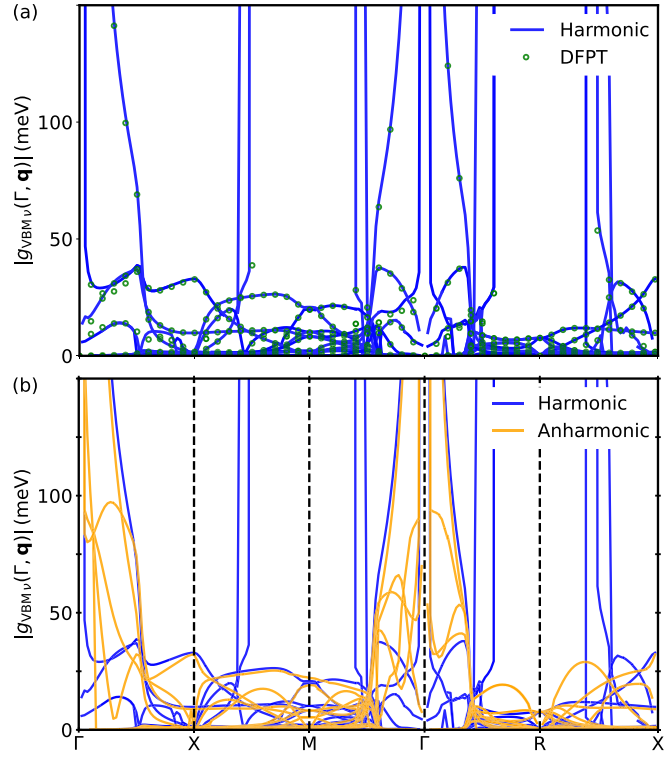

FIG. 3. (a) Comparison between the harmonic electron-phonon matrix elements $|g|$ computed with direct DFPT calculations (green circles) and Fourier-Wannier interpolated using the EPW code (blue lines) at PBE level with SOC considered. (b) Anharmonic effect at 300 K computed with TDEP and Fourier-interpolated with EPW (orange lines) compared with harmonic interpolation (blue lines). The matrix elements are shown for the valence band maximum (VBM) along the phonon momentum **q** and for all phonon branches ν.

with Fourier-Wannier interpolated results in Fig. 3(a) along high-symmetry lines, showing good agreement. Matrix elements diverge at points $\mathbf{q} = M$ and $\mathbf{q} = R$ due to soft modes in Fig. 2. As $CsSnBr_3$ is polar, it exhibits a Fröhlich divergence of $|g_{mn\nu}(\mathbf{k}, \mathbf{q})|$ due to LO mode interactions, noted in $|\mathbf{q}| \to 0$. Previous studies highlight quadrupoles' role in $g_{mn\nu}(\mathbf{k}, \mathbf{q})$ calculations [77,78]. Dynamical quadrupoles occur in noncentrosymmetric crystals and can also be present in centrosymmetric ones with noncentrosymmetric sites [79]. Since $CsSnBr_3$ has spatial inversion symmetry, quadrupoles are zero, explaining the good fit in Fig. 3(a) without quadrupolar corrections.

We used the effective interatomic force constants from TDEP at 300 K, interpolating them with Wannier-Fourier, as shown in Fig. 3(b). Comparing these interpolated elements to the harmonic ones reveals finite values around the $\mathbf{q} = M$ and R points and a notable increase near the zone center, except for the Fröhlich longitudinal optical mode. This increase in $|g_{mn\nu}(\mathbf{k}, \mathbf{q})|$ leads to higher scattering rates and reduced mobility. Figures S4 and S5 of the SM [63] show the matrix elements and different temperatures and find that anharmonicity increases the electron-phonon coupling by 20.9%, 22%, and 22.3% at 300, 400, and 500 K, respectively. We then compute the drift and Hall transport properties of $CsSnBr_3$ by solving the BTE, starting from a $6 \times 6 \times 6$ coarse **k** and **q**

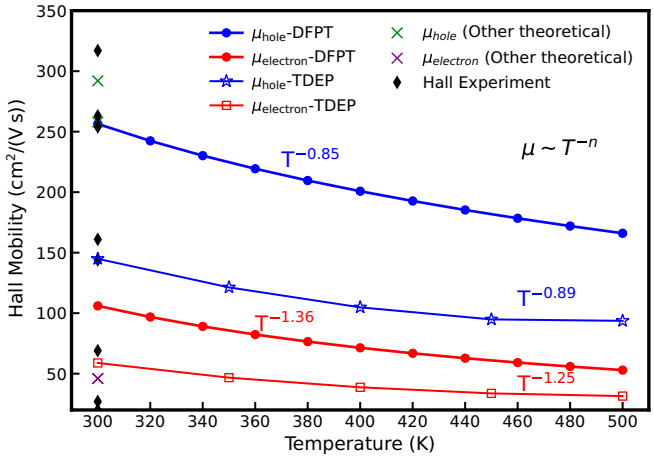

FIG. 4. Hall mobility calculated using an electronic band structure at the HSE06 level with SOC. The blue (hole) and red (electron) dots and lines represent results from harmonic DFPT-calculated phonon dispersions, while the blue stars (hole) and red squares (electron) correspond to anharmonic results from TDEP-calculated phonon dispersions. The temperature exponent of the Hall mobility is also reported. Experimental Hall data are from Ref. [80] and theoretical data from Refs. [81–84].

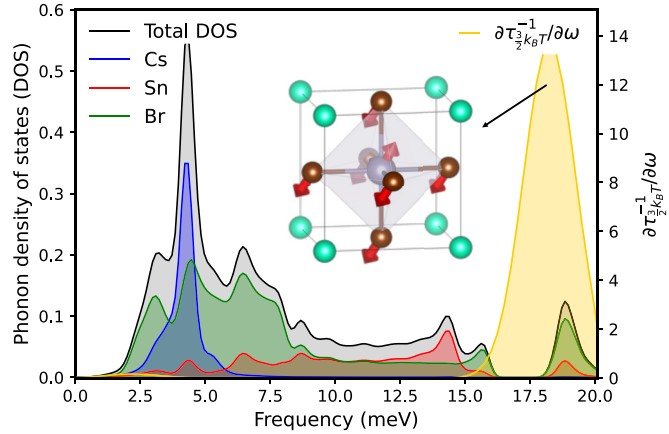

FIG. 5. Projected phonon density states (gray, blue, red, and green), hole spectral decomposition of the scattering rates (orange), and displacement vectors for the phonon mode associated with the peak located around 18 meV.

grid and interpolating onto a fine 80 × 80 × 80 **k** and **q** grid. Figure 4 shows the temperature-dependent carrier mobility of $CsSnBr_3$, calculated via the iterative Hall BTE approach with the Lorenz force due to a vanishing magnetic field [68]. As the cubic phase of $CsSnBr_3$ is stable above 292 K, we concentrate on data from 300 to 500 K. Accurate carrier mobility calculations depend on a precise electronic band edge description. PBE calculations, both with and without SOC, underestimate the band gap, enhancing VBM and CBM coupling and resulting in nonparabolic band edges. In contrast, HSE06 with SOC provides a more accurate description of the parabolic band edges. Therefore, our mobility calculations and the subsequent discussion are based on the HSE06 results. We report the mobilities obtained with PBE calculations in Table S1 of the SM [63] as well as a comparison to prior works in Table S2. Hall hole mobility surpasses electron mobility in both harmonic and anharmonic calculations. Introducing anharmonic effects reduces mobilities, though temperature dependence changes minimally. Harmonic phonons neglect soft modes in BTE solutions, overestimating mobilities. At room temperature, Hall electron and hole mobilities are 106 and 256 $cm^2/(Vs)$, respectively; with anharmonicity, they decrease to 59 and 145 $cm^2/(Vs)$. Drift mobility calculations (see Table S3 of the SM [63]) showed slightly lower values, indicating a Hall factor range of 1.16 to 1.19 for holes and 1.1 to 1.13 for electrons. Figure 5 presents the spectral decomposition showing that the strongest electron-phonon coupling occurs at the highest LO mode, which contributes significantly to the scattering processes and is a common feature of many perovskites [10,85]. This causes the low carrier mobility, linked to the Pb-Br stretching modes. Nonetheless, our results fall within the experimental range. By fitting carrier mobility against T^{-n} following the T^n power law from 300 to 500 K, we determine $n = 0.89$ for holes and 1.25 for electrons with TDEP, and $n = 0.85$ for holes and 1.36 with DFPT. Calculations considering thermal volume expansion based on an experimental thermal expansion coefficient are discussed in the SM [63], which shows that stronger scattering induced by the volume expansion will further lower the carrier mobility.

Overall, we developed a workflow for studying electron-phonon interactions and carrier transport in anharmonic materials. Our calculations indicate that neglecting anharmonic effects leads to major errors in predicting carrier mobility, particularly in materials with dynamic disorder and strong anharmonic interactions. In $CsSnBr_3$, carrier mobility is mainly limited by electron-phonon scattering from the LO phonon mode. Anharmonic effects reduce carrier mobility by 44% for holes and 43% for electrons due to increased electron-phonon coupling. The Hall factor is weakly dependent on temperature, around 1.1, suggesting similar results in Hall and time-of-flight experiments. This work aids future research on perovskites and anharmonic systems.

S.P. acknowledges support from the Fonds de la Recherche Scientifique de Belgique (FRS-FNRS). This work was supported by the Fonds de la Recherche Scientifique-FNRS under Grants No. T.0183.23 (PDR) and No. T.W011.23 (PDR-WEAVE). This publication was supported by the Walloon Region in the strategic axe FRFS-WEL-T. Computational resources have been provided by the PRACE award granting access to MareNostrum4 at Barcelona Supercomputing Center (BSC), Spain, and Discoverer in SofiaTech, Bulgaria (OptoSpin Project ID No. 2020225411), by the EuroHPC JU award granting access to MareNostrum5 at Barcelona Supercomputing Center (BSC), Spain (Project ID No. EHPC-EXT-2023E02-050), and by the Consortium des Équipements de Calcul Intensif (CÉCI), funded by the FRS-FNRS under Grant No. 2.5020.11, by the Tier-1 supercomputer of the Walloon Region (Lucia) with infrastructure funded by the Walloon Region under the Grant Agreement No. 1910247.

Data Availability. The data that support the findings of this article are openly available [86].

[1] S. D. Stranks and H. J. Snaith, Metal-halide perovskites for photovoltaic and light-emitting devices, Nat. Nanotechnol. **10**, 391 (2015).

[2] Y. Rong, Y. Hu, A. Mei, H. Tan, M. I. Saidaminov, S. I. Seok, M. D. McGehee, E. H. Sargent, and H. Han, Challenges for commercializing perovskite solar cells, Science **361**, eaat8235 (2018).

[3] W. Nie, H. Tsai, R. Asadpour, J.-C. Blancon, A. J. Neukirch, G. Gupta, J. J. Crochet, M. Chhowalla, S. Tretiak, M. A. Alam, H.-L. Wang, and A. D. Mohite, High-efficiency solution-processed perovskite solar cells with millimeter-scale grains, Science **347**, 522 (2015).

[4] S. Kumar, S. S. Sharma, J. Giri, E. Makki, T. Sathish, and H. Panchal, Perovskite materials with improved stability and environmental friendliness for photovoltaics, Front. Mech. Eng. **10**, 1 (2024).

[5] C. E. Torrence, C. S. Libby, W. Nie, and J. S. Stein, Environmental and health risks of perovskite solar modules: Case for better test standards and risk mitigation solutions, iScience **26**, 105807 (2023).

[6] M. Ren, X. Qian, Y. Chen, T. Wang, and Y. Zhao, Potential lead toxicity and leakage issues on lead halide perovskite photovoltaics, J. Hazardous Mater. **426**, 127848 (2022).

[7] X. Liu, K. Yan, D. Tan, X. Liang, H. Zhang, and W. Huang, Solvent engineering improves efficiency of lead-free tin-based hybrid perovskite solar cells beyond 9%, ACS Energy Lett. **3**, 2701 (2018).

[8] L. M. Herz, Charge-carrier mobilities in metal halide perovskites: Fundamental mechanisms and limits, ACS Energy Lett. **2**, 1539 (2017).

[9] T. M. Brenner, D. A. Egger, A. M. Rappe, L. Kronik, G. Hodes, and D. Cahen, Are mobilities in hybrid organic–inorganic halide perovskites actually high? J. Phys. Chem. Lett. **6**, 4754 (2015).

[10] S. Poncé, M. Schlipf, and F. Giustino, Origin of low carrier mobilities in halide perovskites, ACS Energy Lett. **4**, 456 (2019).

[11] C. Q. Xia, J. Peng, S. Poncé, J. B. Patel, A. D. Wright, T. W. Crothers, M. Uller Rothmann, J. Borchert, R. L. Milot, H. Kraus, Q. Lin, F. Giustino, L. M. Herz, and M. B. Johnston, Limits to electrical mobility in lead-halide perovskite semiconductors, J. Phys. Chem. Lett. **12**, 3607 (2021).

[12] Q. Tao, P. Xu, M. Li, and W. Lu, Machine learning for perovskite materials design and discovery, npj Comput. Mater. **7**, 23 (2021).

[13] F. Wang, S. Bai, W. Tress, A. Hagfeldt, and F. Gao, Defects engineering for high-performance perovskite solar cells, npj Flex. Electron. **2**, 22 (2018).

[14] X. Gonze and C. Lee, Dynamical matrices, born effective charges, dielectric permittivity tensors, and interatomic force constants from density-functional perturbation theory, Phys. Rev. B **55**, 10355 (1997).

[15] S. Baroni, S. de Gironcoli, A. Dal Corso, and P. Giannozzi, Phonons and related crystal properties from density-functional perturbation theory, Rev. Mod. Phys. **73**, 515 (2001).

[16] W. M. C. Foulkes, L. Mitas, R. J. Needs, and G. Rajagopal, Quantum Monte Carlo simulations of solids, Rev. Mod. Phys. **73**, 33 (2001).

[17] R. Iftimie, P. Minary, and M. E. Tuckerman, *Ab initio* molecular dynamics: Concepts, recent developments, and future trends, Proc. Natl. Acad. Sci. USA **102**, 6654 (2005).

[18] X.-G. Zhao, G. M. Dalpian, Z. Wang, and A. Zunger, Polymorphous nature of cubic halide perovskites, Phys. Rev. B **101**, 155137 (2020).

[19] M. Zacharias, G. Volonakis, F. Giustino, and J. Even, Anharmonic electron-phonon coupling in ultrasoft and locally disordered perovskites, npj Comput. Mater. **9**, 153 (2023).

[20] M. Zacharias, G. Volonakis, F. Giustino, and J. Even, Anharmonic lattice dynamics via the special displacement method, Phys. Rev. B **108**, 035155 (2023).

[21] Y. Wang, M. Zacharias, X. Zhang, N. Pant, J. Even, P. F. P. Poudeu, and E. Kioupakis, Efficient first-principles framework for overdamped phonon dynamics and anharmonic electron-phonon coupling in superionic materials, Phys. Rev. Lett. **135**, 056402 (2025).

[22] A. Zunger, Bridging the gap between density functional theory and quantum materials, Nat. Comput. Sci. **2**, 529 (2022).

[23] J.-X. Xiong, X. Zhang, and A. Zunger, Role of magnetic and structural symmetry breaking in forming the Mott insulating gap in Nb_3Cl_8, Phys. Rev. B **111**, 155122 (2025).

[24] I. Errea, M. Calandra, and F. Mauri, Anharmonic free energies and phonon dispersions from the stochastic self-consistent harmonic approximation: Application to platinum and palladium hydrides, Phys. Rev. B **89**, 064302 (2014).

[25] T. Tadano and S. Tsuneyuki, First-principles lattice dynamics method for strongly anharmonic crystals, J. Phys. Soc. Jpn. **87**, 041015 (2018).

[26] B. Monserrat, N. D. Drummond, and R. J. Needs, Anharmonic vibrational properties in periodic systems: Energy, electron-phonon coupling, and stress, Phys. Rev. B **87**, 144302 (2013).

[27] M. Lazzeri and S. de Gironcoli, First-principles study of the thermal expansion of Be101¯0, Phys. Rev. B **65**, 245402 (2002).

[28] L. Paulatto, F. Mauri, and M. Lazzeri, Anharmonic properties from a generalized third-orderab initioapproach: Theory and applications to graphite and graphene, Phys. Rev. B **87**, 214303 (2013).

[29] O. Hellman, I. A. Abrikosov, and S. I. Simak, Lattice dynamics of anharmonic solids from first principles, Phys. Rev. B **84**, 180301(R) (2011).

[30] L. Monacelli, R. Bianco, M. Cherubini, M. Calandra, I. Errea, and F. Mauri, The stochastic self-consistent harmonic approximation: Calculating vibrational properties of materials with full quantum and anharmonic effects, J. Phys.: Condens. Matter **33**, 363001 (2021).

[31] O. Hellman and I. A. Abrikosov, Temperature-dependent effective third-order interatomic force constants from first principles, Phys. Rev. B **88**, 144301 (2013).

[32] F. Knoop, N. Shulumba, A. Castellano, J. P. A. Batista, R. Farris, M. J. Verstraete, M. Heine, D. Broido, D. S. Kim, J. Klarbring, I. A. Abrikosov, S. I. Simak, and O. Hellman, TDEP: Temperature dependent effective potentials, J. Open Source Software **9**, 6150 (2024).

[33] A. Togo, L. Chaput, and I. Tanaka, Distributions of phonon lifetimes in Brillouin zones, Phys. Rev. B **91**, 094306 (2015).

[34] A. Togo, L. Chaput, T. Tadano, and I. Tanaka, Implementation strategies in phonopy and phono3py, J. Phys.: Condens. Matter **35**, 353001 (2023).

[35] D. A. Broido, M. Malorny, G. Birner, N. Mingo, and D. A. Stewart, Intrinsic lattice thermal conductivity of

semiconductors from first principles, Appl. Phys. Lett. **91**, 231922 (2007).

[36] F. Zhou, W. Nielson, Y. Xia, and V. Ozoliņš, Lattice anharmonicity and thermal conductivity from compressive sensing of first-principles calculations, Phys. Rev. Lett. **113**, 185501 (2014).

[37] T. Tadano and S. Tsuneyuki, Self-consistent phonon calculations of lattice dynamical properties in cubic $SrTiO_3$ with first-principles anharmonic force constants, Phys. Rev. B **92**, 054301 (2015).

[38] T. Tadano, Y. Gohda, and S. Tsuneyuki, Anharmonic force constants extracted from first-principles molecular dynamics: Applications to heat transfer simulations, J. Phys.: Condens. Matter **26**, 225402 (2014).

[39] R. Masuki, T. Nomoto, R. Arita, and T. Tadano, Full optimization of quasiharmonic free energy with an anharmonic lattice model: Application to thermal expansion and pyroelectricity of wurtzite GaN and ZnO, Phys. Rev. B **107**, 134119 (2023).

[40] P. Souvatzis, O. Eriksson, M. I. Katsnelson, and S. P. Rudin, Entropy driven stabilization of energetically unstable crystal structures explained from first principles theory, Phys. Rev. Lett. **100**, 095901 (2008).

[41] F. Eriksson, E. Fransson, and P. Erhart, The hiphive package for the extraction of high-order force constants by machine learning, Adv. Theory Simul. **2**, 1800184 (2019).

[42] M. Zacharias and F. Giustino, Theory of the special displacement method for electronic structure calculations at finite temperature, Phys. Rev. Res. **2**, 013357 (2020).

[43] F. Bottin, J. Bieder, and J. Bouchet, A-TDEP: Temperature dependent effective potential for ABINIT–lattice dynamic properties including anharmonicity, Comput. Phys. Commun. **254**, 107301 (2020).

[44] M. S. Green, Markoff random processes and the statistical mechanics of time-dependent phenomena. II. Irreversible processes in fluids, J. Chem. Phys. **22**, 398 (1954).

[45] R. Kubo, Statistical-mechanical theory of irreversible processes. I. General theory and simple applications to magnetic and conduction problems, J. Phys. Soc. Jpn. **12**, 570 (1957).

[46] J.-M. Lihm and S. Poncé, Nonperturbative self-consistent electron-phonon spectral functions and transport, Phys. Rev. Lett. **134**, 186401 (2025).

[47] S. Poncé, W. Li, S. Reichardt, and F. Giustino, First-principles calculations of charge carrier mobility and conductivity in bulk semiconductors and two-dimensional materials, Rep. Prog. Phys. **83**, 036501 (2020).

[48] R. Claes, S. Poncé, G.-M. Rignanese, and G. Hautier, Phonon-limited electronic transport through first principles, Nat. Rev. Phys. **7**, 73 (2025).

[49] S. Poncé, E. Margine, C. Verdi, and F. Giustino, EPW: Electron–phonon coupling, transport and superconducting properties using maximally localized wannier functions, Comput. Phys. Commun. **209**, 116 (2016).

[50] H. Lee, S. Poncé, K. Bushick, S. Hajinazar, J. Lafuente-Bartolome, J. Leveillee, C. Lian, J.-M. Lihm, F. Macheda, H. Mori, H. Paudyal, W. H. Sio, S. Tiwari, M. Zacharias, X. Zhang, N. Bonini, E. Kioupakis, E. R. Margine, and F. Giustino, Electron–phonon physics from first principles using the EPW code, npj Comput. Mater. **9**, 156 (2023).

[51] J. Quan, C. Carbogno, and M. Scheffler, Carrier mobility of strongly anharmonic materials from first principles, Phys. Rev. B **110**, 235202 (2024).

[52] M. J. Schilcher, D. J. Abramovitch, M. Z. Mayers, L. Z. Tan, D. R. Reichman, and D. A. Egger, Correlated anharmonicity and dynamic disorder control carrier transport in halide perovskites, Phys. Rev. Mater. **7**, L081601 (2023).

[53] J.-J. Zhou, O. Hellman, and M. Bernardi, Electron-Phonon scattering in the presence of soft modes and electron mobility in $SrTiO_3$ perovskite from first principles, Phys. Rev. Lett. **121**, 226603 (2018).

[54] L. Ranalli, C. Verdi, M. Zacharias, J. Even, F. Giustino, and C. Franchini, Electron mobilities in $SrTiO_3$ and $KTaO_3$: Role of phonon anharmonicity, mass renormalization, and disorder, Phys. Rev. Mater. **8**, 104603 (2024).

[55] K.-C. Zhang, C. Shen, H.-B. Zhang, Y.-F. Li, and Y. Liu, Effect of quartic anharmonicity on the carrier transport of cubic halide perovskites $CsSnI_3$ and $CsPbI_3$, Phys. Rev. B **106**, 235202 (2022).

[56] J.-C. Zheng, C. H. A. Huan, A. T. S. Wee, and M. H. Kuok, Electronic properties of $CsSnBr_3$: Studies by experiment and theory, Surf. Interface Anal. **28**, 81 (1999).

[57] M. Coduri, T. A. Strobel, M. Szafrański, A. Katrusiak, A. Mahata, F. Cova, S. Bonomi, E. Mosconi, F. De Angelis, and L. Malavasi, Band gap engineering in $MASnBr_3$ and $CsSnBr_3$ perovskites: Mechanistic insights through the application of pressure, J. Phys. Chem. Lett. **10**, 7398 (2019).

[58] P. Giannozzi, O. Andreussi, T. Brumme, O. Bunau, M. Buongiorno Nardelli, M. Calandra, R. Car, C. Cavazzoni, D. Ceresoli, M. Cococcioni, N. Colonna, I. Carnimeo, A. Dal Corso, S. de Gironcoli, P. Delugas, R. A. DiStasio, A. Ferretti, A. Floris, G. Fratesi, G. Fugallo *et al.*, Advanced capabilities for materials modeling with QUANTUM ESPRESSO, J. Phys.: Condens. Matter **29**, 465901 (2017).

[59] D. R. Hamann, Optimized norm-conserving Vanderbilt pseudopotentials, Phys. Rev. B **88**, 085117 (2013).

[60] J. P. Perdew, K. Burke, and M. Ernzerhof, Generalized gradient approximation made simple, Phys. Rev. Lett. **77**, 3865 (1996).

[61] M. J. van Setten, M. Giantomassi, X. Gonze, G.-M. Rignanese, and G. Hautier, Automation methodologies and large-scale validation for *GW*: Towards high-throughput *GW* calculations, Phys. Rev. B **96**, 155207 (2017).

[62] J. Heyd, G. E. Scuseria, and M. Ernzerhof, Hybrid functionals based on a screened Coulomb potential, J. Chem. Phys. **118**, 8207 (2003).

[63] See Supplemental Material at http://link.aps.org/supplemental/10.1103/yssy-5t2v for convergence studies, additional information, and the impact of thermal expansion, which includes Refs. [70,82,83,84,87].

[64] N. Shulumba, O. Hellman, and A. J. Minnich, Intrinsic localized mode and low thermal conductivity of PbSe, Phys. Rev. B **95**, 014302 (2017).

[65] N. Shulumba, O. Hellman, and A. J. Minnich, Lattice thermal conductivity of polyethylene molecular crystals from first-principles including nuclear quantum effects, Phys. Rev. Lett. **119**, 185901 (2017).

[66] M. Mori and H. Saito, An x-ray study of successive phase transitions in $CsSnBr_3$, J. Phys. C: Solid State Phys. **19**, 2391 (1986).

[67] S. Poncé, E. R. Margine, and F. Giustino, Towards predictive many-body calculations of phonon-limited carrier mobilities in semiconductors, Phys. Rev. B **97**, 121201(R) (2018).

[68] S. Poncé, F. Macheda, E. R. Margine, N. Marzari, N. Bonini, and F. Giustino, First-principles predictions of Hall and drift mobilities in semiconductors, Phys. Rev. Res. **3**, 043022 (2021).

[69] F. Giustino, Electron-phonon interactions from first principles, Rev. Mod. Phys. **89**, 015003 (2017).

[70] D. H. Fabini, G. Laurita, J. S. Bechtel, C. C. Stoumpos, H. A. Evans, A. G. Kontos, Y. S. Raptis, P. Falaras, A. Van der Ven, M. G. Kanatzidis, and R. Seshadri, Dynamic stereochemical activity of the Sn^{2+} lone pair in perovskite $CsSnBr_3$, J. Am. Chem. Soc. **138**, 11820 (2016).

[71] S. Gupta, T. Bendikov, G. Hodes, and D. Cahen, $CsSnBr_3$, a lead-free halide perovskite for long-term solar cell application: Insights on Sn^{2+} Addition, ACS Energy Lett. **1**, 1028 (2016).

[72] I. B. Garba, L. Trombini, C. Katan, J. Even, M. Zacharias, M. Kepenekian, and G. Volonakis, Three-dimensional to layered halide perovskites: A parameter-free hybrid functional method for predicting electronic band gaps, ACS Mater. Lett. **7**, 1922 (2025).

[73] S. Poncé, Y. Gillet, J. Laflamme Janssen, A. Marini, M. Verstraete, and X. Gonze, Temperature dependence of the electronic structure of semiconductors and insulators, J. Chem. Phys. **143**, 102813 (2015).

[74] J.-M. Lihm and S. Poncé, Beyond-quasiparticles transport with vertex correction: Self-consistent ladder formalism for electron-phonon interactions, arXiv:2506.18139.

[75] X. Gonze, J.-C. Charlier, D. C. Allan, and M. P. Teter, Interatomic force constants from first principles: The case of a-quartz, Phys. Rev. B **50**, 13035 (1994).

[76] F. Giustino, M. L. Cohen, and S. G. Louie, Electron-phonon interaction using Wannier functions, Phys. Rev. B **76**, 165108 (2007).

[77] G. Brunin, H. P. C. Miranda, M. Giantomassi, M. Royo, M. Stengel, M. J. Verstraete, X. Gonze, G.-M. Rignanese, and G. Hautier, Electron-phonon beyond Fröhlich: Dynamical quadrupoles in polar and covalent solids, Phys. Rev. Lett. **125**, 136601 (2020).

[78] S. Poncé, M. Royo, M. Gibertini, N. Marzari, and M. Stengel, Accurate prediction of Hall mobilities in two-dimensional materials through gauge-covariant quadrupolar contributions, Phys. Rev. Lett. **130**, 166301 (2023).

[79] V. A. Jhalani, J.-J. Zhou, J. Park, C. E. Dreyer, and M. Bernardi, Piezoelectric electron-phonon interaction from *ab initio* dynamical quadrupoles: Impact on charge transport in Wurtzite GaN, Phys. Rev. Lett. **125**, 136602 (2020).

[80] J. Jia, R. Wang, and H. Mu, Exciton dynamics and photoresponse behavior of the *in situ* annealed $CsSnBr_3$ perovskite films synthesized by thermal evaporation, Nanotechnology **33**, 345503 (2022).

[81] L. Y. Huang and W. R. L. Lambrecht, Electronic band structure, phonons, and exciton binding energies of halide perovskites cssncl, Phys. Rev. B **88**, 165203 (2013).

[82] S. Cao, Y. Su, K.-K. Song, P. Qian, Y. Yan, and L.-B. Shi, Biaxial strain improving carrier mobility for inorganic perovskite: *Ab initio* Boltzmann transport equation, J. Phys.: Condens. Matter **35**, 055702 (2022).

[83] Y. Su, H. Wang, L.-B. Shi, Y.-Z. Wang, Q. Liu, and P. Qian, An investigation on carrier transport behavior of tetragonal halide perovskite: First-principles calculation, Mater. Sci. Semicond. Process. **150**, 106836 (2022).

[84] X. Zeng, G. Niu, X. Wang, J. Jiang, L. Sui, Y. Zhang, A. Chen, M. Jin, K. Yuan, and X. Yang, Enhanced carrier transport in Cs_xSnBr_y perovskite by reducing electron-phonon coupling under compressive strain, Mater. Today Phys. **40**, 101296 (2024).

[85] B. Cucco, J. Leveillee, V.-A. Ha, J. Even, M. Kepenekian, F. Giustino, and G. Volonakis, Intrinsic limits of charge carrier mobilities in layered halide perovskites, PRX Energy **3**, 023012 (2024).

[86] J. Yin, O. Hellman, and S. Poncé, "Impact of anharmonicity on the carrier mobility of the pb-free $CsSnBr_3$ (2025)", Materials Cloud Archive, https://doi.org/10.24435/materialscloud:3e-s3.

[87] Y. Zhang, Q. Yao, J. Qian, X. Zhao, D. Li, and Q. Mi, Thermoelectric properties of all-inorganic perovskite $CsSnBr_3$: A combined experimental and theoretical study, Chem. Phys. Lett. **754**, 137637 (2020).